



Cite this: *Phys. Chem. Chem. Phys.*,  
2016, 18, 30721

# Tuning the vibrational coupling of $\text{H}_3\text{O}^+$ by changing its solvation environment†

Jake A. Tan,<sup>abc</sup> Jheng-Wei Li,<sup>ad</sup> Cheng-chau Chiu,<sup>a</sup> Hsin-Yi Liao,<sup>e</sup> Hai Thi Huynh<sup>a</sup>  
and Jer-Lai Kuo<sup>‡\*acd</sup>

This study demonstrates how the intermode coupling in the hydronium ion ( $\text{H}_3\text{O}^+$ ) is modulated by the composition of the first solvation shell. A series of rare gas solvated hydronium ions ( $\text{H}_3\text{O}^+\text{Rg}_3$ , where  $\text{Rg} = \text{Ne}, \text{Ar}, \text{Kr}, \text{and Xe}$ ) is examined via reduced-dimensional anharmonic vibrational (RDAV) *ab initio* calculations. We considered six key vibrational normal modes, namely: a hindered rotation, two H–O–H bends, and three O–H stretches. Between the O–H stretches and the H–O–H bends, the first is more sensitive to solvation strength. Our calculations revealed that the Fermi resonance between the first overtones of O–H bends and the fundamentals of O–H stretches led to complex spectral features from 3000 to 3500  $\text{cm}^{-1}$ . Such an interaction is not only sensitive to the type of rare gas messengers surrounding the  $\text{H}_3\text{O}^+$  ion, it also exhibits an anomalous  $\text{H} \rightarrow \text{D}$  isotope effect. Although it is accepted that visible combination tones ( $\sim 1900 \text{ cm}^{-1}$ ) arise from the complex coupling between the hindered rotation and the H–O–H bends, the origin of their intensities is not yet clearly understood. We found that the intensity of these combination tones could be much stronger than their fundamental H–O–H bends. Within our theoretical framework, we tracked the combination tone's intensity back to the asymmetric O–H stretches. This simple notion of intensity borrowing is confirmed by examining eight complexes ( $\text{H}_3\text{O}^+\cdot\text{Rg}_3$  and  $\text{D}_3\text{O}^+\cdot\text{Rg}_3$ ) with spectral features awaiting experimental confirmations.

Received 14th September 2016,  
Accepted 14th October 2016

DOI: 10.1039/c6cp06326h

www.rsc.org/pccp

## 1. Introduction

Due to the importance of solvated protons ( $\text{H}^+$ ) in chemistry and biology,<sup>1–6</sup> there is an on-going debate on whether aqueous protons are dominated by the Eigen ( $\text{H}_3\text{O}^+$ ) or Zundel ( $\text{H}_5\text{O}_2^+$ ) species. A clear identification of the main vibrational signatures of each species is certainly essential to conclude this controversy. Both infrared multiple photon dissociation (IRMPD)<sup>7–10</sup> and messenger tagged infrared predissociation (IRPD)<sup>11–28</sup> spectroscopy have been extensively used to probe the vibrational realm

of both species in the gas phase. However, substantial anharmonic effects, as well as significant nuclear quantum effects often lead to a complex vibrational spectrum – demanding sophisticated techniques beyond the harmonic approximation to understand them.

For example, the enigmatic doublet around 1000  $\text{cm}^{-1}$  in the action spectrum of  $\text{H}_5\text{O}_2^+\cdot\text{Ne}$  had solicited considerable efforts to uncover its identity.<sup>16,20,21,29,30</sup> Full-dimensional calculations by Vendrell and co-workers<sup>31–35</sup> attributed this doublet to the coupling between the bright proton transfer mode and a combination tone involving the O–O stretch and a water wagging mode. Furthermore, in some Zundel systems, the proton transfer mode may couple with the nearby flanking modes. One recently reported case was  $\text{H}^+(\text{MeOH})_2$  in which the asymmetric C–O stretch and the in-plane methyl rock strongly couples with the proton transfer mode leading to a “triplet” feature in the range 800–1200  $\text{cm}^{-1}$ .<sup>36,37</sup>

The simplest solvated proton, the hydronium ion,  $\text{H}_3\text{O}^+$ , has been studied experimentally by Lee's group.<sup>12</sup> In 1989, they reported the vibrational spectra of  $\text{H}_3\text{O}^+(\text{H}_2)_n$  ( $n = 1–3$ ) in the range 3000–4000  $\text{cm}^{-1}$ . *Ab initio* molecular dynamics (AIMD) simulations have been utilized by Baer and co-workers<sup>38</sup> to simulate these clusters, but an understanding of the messenger effects toward the partially rotational resolved O–H stretches is still far from complete. In 2010, Duncan's group<sup>39</sup> measured

<sup>a</sup> Institute of Atomic and Molecular Sciences, Academia Sinica,  
No. 1 Roosevelt Road, Section 4, Da-an District, Taipei 10617, Taiwan,  
Republic of China. E-mail: jlkuo@pub.iam.s.sinica.edu.tw

<sup>b</sup> Department of Chemistry, National Tsing Hua University, No. 101 Kuang-Fu Road,  
Section 2, Hsinchu 30013, Taiwan, Republic of China

<sup>c</sup> Molecular Science and Technology Program, Taiwan International Graduate  
Program, Academia Sinica, No. 128 Academia Road, Section 2, Nangang District,  
Taipei 11529, Taiwan, Republic of China

<sup>d</sup> Department of Physics, National Taiwan University, No. 1 Roosevelt Road,  
Section 4, Taipei 10617, Taiwan, Republic of China

<sup>e</sup> Department of Science Education, National Taipei University of Education,  
No. 134, Section 2, Heping E. Rd., Da-an District, Taipei City 10671, Taiwan,  
Republic of China

† Electronic supplementary information (ESI) available. See DOI: 10.1039/c6cp06326h

‡ Present address: Institute of Atomic and Molecular Sciences, Academia Sinica,  
No. 1 Roosevelt Road, Section 4, Da-an District, Taipei 10617, Taiwan, Republic of China.

and examined the O–H stretches of  $\text{H}_3\text{O}^+(\text{N}_2)_n$  ( $n = 1-3$ ). Harmonic calculations were performed to assist their assignment. They identified a combination band between the O–H stretches and the low-frequency intermolecular stretches. In 2012, Johnson's group recorded the vibrational spectra of  $\text{H}_3\text{O}^+\cdot\text{Ar}_n$  ( $n = 1-3$ ) covering a wider frequency window ranging from 1500 to  $3800\text{ cm}^{-1}$ .<sup>19,40</sup> This spectral range contains sharp and intense bands corresponding to O–H stretches, H–O–H bends, and some combination bands. Recently, we reported our six-dimensional calculations (RDAV-6D) on  $\text{H}_3\text{O}^+\cdot\text{Ar}_n$  ( $n = 1-3$ ) with an emphasis on how the vibrational features can be modulated by the number of messenger atoms.<sup>41</sup> Our RDAV-6D calculations included one hindered rotation, two H–O–H bends, and three O–H stretches. This managed to explain most of the dominant features in Johnson's IRPD spectrum.<sup>19</sup>

We fully subscribe to the idea that agreement between experimental data and theoretical calculations must not be the end of any simulation. We believed that such agreement is just the beginning of a deeper understanding.<sup>42</sup> Thus, we are motivated to use different species of rare gas messengers to tune the solvation environment of the Eigen ion ( $\text{H}_3\text{O}^+$ ). This time, we aim to gain further insights into the vibrational coupling and sought for experimentally observable spectral features. It is well documented in the literature<sup>17,19,20</sup> that IRPD assisted by rare gas tagging provides a sharper and clearer spectrum. The possibility to have a well-resolved experimental spectrum will make the comparison more straightforward and less ambiguous. Furthermore, the effect of the rare gas (Ne, Ar, Kr, and Xe) messengers on the IR spectra of protonated clusters has also been thoroughly studied by several experimental groups.<sup>13,14,25,43,44</sup> Among the rare gas messengers in this study, Ne is considered to be the least perturbing, while Xe is the most perturbing messenger. Moreover, Xe messenger is capable of inducing additional bands other than those arising from the six modes mentioned above.<sup>43,44</sup> In this work, we will focus on investigating the vibrational signatures of Ne, Ar, Kr, and Xe-tagged  $\text{H}_3\text{O}^+$ . Since nuclear quantum effects cannot be probed directly by experiments, we have also computed the totally deuterated isotopologues (Ne, Ar, Kr, and Xe-tagged  $\text{D}_3\text{O}^+$ ) to examine H  $\rightarrow$  D isotope effects.

The rest of the paper is organized in the following manner. In Section 2, we briefly describe our theoretical methods. In Section 3, we begin by presenting the symmetry of the minimum structure followed by the evolution of  $\text{H}_3\text{O}^+\cdot\text{Rg}_3$ 's spectrum across the rare gas congeners. Lastly, we provide a brief conclusion in Section 4.

## 2. Theoretical methods

All *ab initio* calculations were performed using the Gaussian 09 suite of programs Rev. D.01.<sup>45</sup> Similar to our previous work<sup>41</sup> on  $\text{H}_3\text{O}^+\cdot\text{Ar}_n$  ( $n = 1-3$ ), the MP2 method<sup>46</sup> was utilized in this study. Our whole computational strategy together with the analysis techniques is summarized as follows. The singlet-ground state of  $\text{H}_3\text{O}^+\cdot\text{Rg}_3$  underwent a full geometry optimization (minimization). The MP2/aug-cc-pVDZ was used for  $\text{H}_3\text{O}^+\cdot\text{Ne}_3$  and  $\text{H}_3\text{O}^+\cdot\text{Ar}_3$ ,

while MP2/aug-cc-pVDZ-PP was used for  $\text{H}_3\text{O}^+\cdot\text{Kr}_3$  and  $\text{H}_3\text{O}^+\cdot\text{Xe}_3$ . The latter basis set was obtained from Basis Set Exchange.<sup>47,48</sup> At the minimum structure, their Hessian matrix was calculated. Diagonalization of this matrix yields the normal modes (NMs) in a rectilinear Cartesian representation. From here, six key NMs were selected. These are the hindered rotation ( $\phi$ ), the degenerate H–O–H bends ( $b_1$  and  $b_2$ ), the symmetric O–H stretch ( $s_1$ ), and the asymmetric O–H stretches ( $s_2$  and  $s_3$ ). Their corresponding displacement vectors were used to generate the reduced-dimensional potential energy surface (PES) and the dipole moment surface (DMS). Each complex in this study has its own singular PES and DMS. Afterward, the corresponding reduced-dimensional vibrational Schrödinger equation was solved numerically through the harmonic oscillator discrete variable representation (DVR).<sup>49–52</sup> From the RDAV eigenvectors and the DMS, the transition intensities were evaluated using Fermi's golden rule.<sup>53</sup> Lastly, analysis of the intermode coupling was performed using a direct product basis constructed from the RDAV-1D and the RDAV-2D eigenvectors. The following subsections contain details of the above steps.

### 2.1 Geometry optimization and harmonic normal mode analysis

The minimum structures for  $\text{H}_3\text{O}^+\cdot\text{Rg}_3$  are highly symmetric. As shown in Fig. 1, each of the Rg atoms binds to one hydrogen atom of  $\text{H}_3\text{O}^+$ . Furthermore, it is evident that these structures possess the following symmetry elements: an identity element ( $E$ ), two three-fold rotational axis ( $C_3$  and  $C_3^2$ ), and three vertical mirror planes ( $\sigma_v$ ) (Fig. 1). Therefore,  $\text{H}_3\text{O}^+\cdot\text{Rg}_3$  belongs to the  $C_{3v}$  point group. As per standard techniques in group theory,

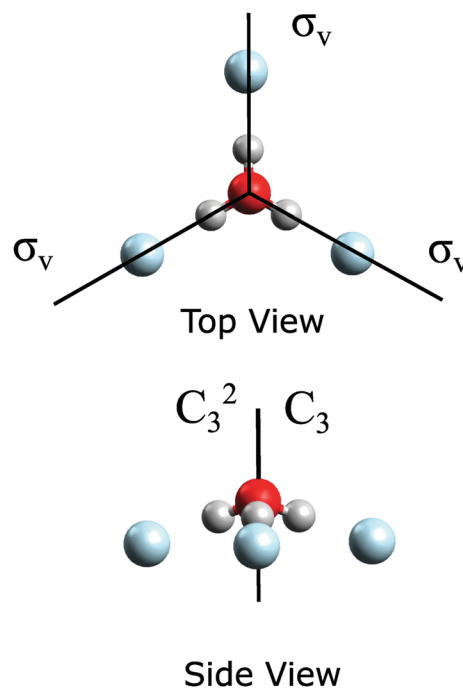


Fig. 1 The symmetry elements of  $\text{H}_3\text{O}^+\cdot\text{Rg}_3$ . The oxygen, hydrogen, and rare gas atoms are represented by red, gray, and blue spheres respectively. The structure belongs to the  $C_{3v}$  point group.

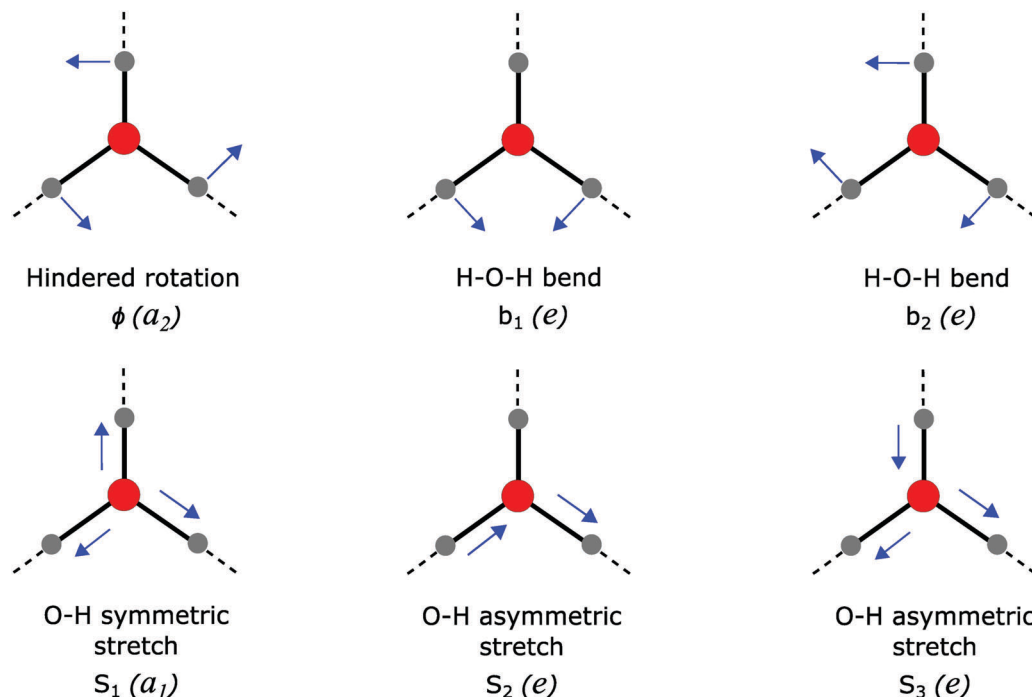


Fig. 2 Schematic representations of the six normal modes of  $\text{H}_3\text{O}^+\cdot\text{Rg}_3$  examined in this work: hindered rotation ( $\phi$ ), bending ( $b_1$  and  $b_2$ ), and stretching ( $s_1$ ,  $s_2$  and  $s_3$ ) modes. Their respective symmetry species are in parenthesis (e.g.  $a_2$  is the symmetry species for  $\phi$ ).

all of the vibrational modes must belong to either  $a_1$ ,  $a_2$ , or  $e$  representation.<sup>54,55</sup> Out of the total fifteen NMs, four modes belong to  $a_1$ , one mode belongs to  $a_2$ , and ten modes belong to  $e$ . Fig. 2 shows a schematic representation of the six key NMs in this study with their respective symmetry species. The reader is advised to pay attention to the manner of symmetry labeling. We fully subscribed to R. S. Mulliken's recommendations<sup>56,57</sup> that lower case letters are used for normal modes, while capital letters are used for vibrational wave functions. The optimized Cartesian coordinates, as well as the determination of symmetry species, can be found in Tables S1 and S2 of the ESI.†

Since our optimizations are conducted in the Born-Oppenheimer<sup>58</sup> approximation, the minimum structure is independent of the isotopic composition. That is, for a given Rg atom, the minimum geometries of  $\text{D}_3\text{O}^+\cdot\text{Rg}_3$  (deuterons) and  $\text{H}_3\text{O}^+\cdot\text{Rg}_3$  (hydrons) are congruent. However, as the atomic masses are parameters of the harmonic normal mode analysis, both their displacement vectors and harmonic frequencies are isotope dependent.<sup>59</sup> With these in mind, we did a normal mode analysis for all  $\text{D}_3\text{O}^+\cdot\text{Rg}_3$  using the minimum geometry of their  $\text{H}_3\text{O}^+\cdot\text{Rg}_3$  counterparts. The harmonic frequencies and their intensities for both hydrons and deuterons can be found in Tables S3 and S4 of the ESI.†

## 2.2 Reduced-dimensional anharmonic vibrational (RDAV) calculations

As mentioned earlier, the vibrational degrees of freedom are described in the rectilinear Cartesian representation. Their displacement vectors were obtained upon diagonalization of the Hessian matrix evaluated at the minimum geometry and

were obtained from Gaussian 09 *via* the keyword freq=hp modes. Visualization of these normal modes shows that their motions are neat. That is, there are no difficulties in classifying these modes as a hindered rotation, a bending mode, or a stretching mode.

Under the NM formalism, the kinetic energy terms are uncoupled, and the potential energy component contains all the anharmonic couplings. By neglecting the contributions from the vibrational angular momentum, the reduced-dimensional vibrational Hamiltonian is written as

$$\hat{H}^{\text{RDAV-6D}} = \frac{-\hbar^2}{2} \left\{ \frac{1}{\mu_\phi} \frac{\partial^2}{\partial q_\phi^2} + \frac{1}{\mu_{b_1}} \frac{\partial^2}{\partial q_{b_1}^2} + \frac{1}{\mu_{b_2}} \frac{\partial^2}{\partial q_{b_2}^2} + \frac{1}{\mu_{s_1}} \frac{\partial^2}{\partial q_{s_1}^2} + \frac{1}{\mu_{s_2}} \frac{\partial^2}{\partial q_{s_2}^2} + \frac{1}{\mu_{s_3}} \frac{\partial^2}{\partial q_{s_3}^2} \right\} + V(q_\phi, q_{b_1}, q_{b_2}, q_{s_1}, q_{s_2}, q_{s_3}) \quad (1)$$

$$\mathbf{H}^{\text{RDAV-6D}} |\Psi_k\rangle = E_k |\Psi_k\rangle \quad (2)$$

where  $\mu_k$  is the effective mass associated with the normal coordinate  $q_k$  and  $V(q_\phi, q_{b_1}, q_{b_2}, q_{s_1}, q_{s_2}, q_{s_3})$  is the 6D PES. The matrix form of the Schrödinger equation is shown in eqn (2) and was solved using the method of discrete variable representation (DVR).<sup>32–35</sup> Several works have reported the success of DVR as a pseudospectral (collocation) approach in studying the vibrational anharmonicity of several systems.<sup>37,41,60,61</sup> In this numerical method, the Hamiltonian in eqn (1) is discretized leading to a matrix in the DVR grid basis. The eigenvalues and eigenvectors are obtained upon matrix diagonalization. Interested readers are advised to refer to the works of Colbert and Miller,<sup>49</sup> as well as

those of Light and co-workers<sup>50–52</sup> for complete characterization of the DVR.

Our DVR implementation is described as follows: the Hermite polynomials were used as basis functions. These polynomials are the harmonic solutions of the six key modes. Then the matrix elements for the kinetic energy operator were calculated using a numerical integration scheme. Gaussian quadrature was used to perform the integration accurately. Using the quadrature points, the PES and DMF were constructed. From here, the Hamiltonian matrix was constructed and diagonalized by a cost-efficient Davidson algorithm.<sup>62</sup>

The relevant information of an absorption spectrum is the transition (1) frequencies and (2) the intensities. The first can be obtained from the eigenvalues referenced to the zero-point energy; while the second can be evaluated from the eigenvectors and the DMS. In this work, we reported our intensities as integrated absorption coefficients ( $A_{f0}$ ) expressed in the SI units of  $\text{km mol}^{-1}$ . Using Fermi's golden rule,<sup>53</sup> we can write

$$A_{f0} = \left( \frac{\pi N_A}{3\epsilon_0 \hbar} \right) \tilde{\nu}_{f0} |\langle \psi_0 | \hat{\mu} | \psi_f \rangle|^2 \quad (3)$$

where  $\psi_0$  and  $\psi_f$  are the initial and the final vibrational states;  $\hat{\mu}$  is the DMS,  $\tilde{\nu}_{f0}$  is the transition energy from  $\psi_0$  to  $\psi_f$ ; and  $\langle \psi_0 | \hat{\mu} | \psi_f \rangle$  is the transition dipole moment. The prefactor in eqn (3) contains the mathematical constant pi ( $\pi$ ), the Avogadro's number ( $N_A$ ), the speed of light in a vacuum ( $c$ ), the vacuum permittivity ( $\epsilon_0$ ), and the reduced Planck's constant ( $\hbar$ ).

In this theoretical framework, we emphasized that there are no arbitrary parameters required other than the set of normal modes included in the RDAV and their number of grid points. The determination of the number of grid points for each normal mode is discussed in Section 2.5.

### 2.3 Exposing the transition's identity via “pure state” (PS) representation

To help us understand the intermode coupling, we will unmask the vibrational state's identity by representing the RDAV-6D eigenvectors from the DVR basis to a “pure state” (PS) basis. The latter representation is defined as the direct products of the eigenvectors from one and two-dimensional cuts of the RDAV-6D. Since arbitrariness is innate in the manner in which the 6D PES is cut, a description of our cutting scheme is necessary. The 6D PES in this study is comprised of two non-degenerate modes:  $q_\phi$  and  $q_{s_1}$ , and two pairs of doubly degenerate modes:  $(q_{b_1}, q_{b_2})$  and  $(q_{s_2}, q_{s_3})$ . To construct the PS basis, we used the one-dimensional (RDAV-1D) anharmonic eigenvectors for the non-degenerate modes and the two-dimensional (RDAV-2D) eigenvectors for the degenerate modes.

One might wonder on the rationale of taking two degenerate modes together (*i.e.* RDAV-2D), and such choice deserves a few words. In the harmonic picture, the 2D PES for a doubly degenerate mode takes the shape of a circular paraboloid. Its isotropic property allows any one-dimensional cut to be degenerate. However, the inclusion of the anharmonicity and the two-mode coupling destroys the isotropic character. As a result, the two 1D cuts on the anharmonic 2D PES must be conducted properly

to preserve degeneracy. Rather than identifying the appropriate cut, we opt to treat these degenerate modes together. In that way, we avoid the dilemma of making the appropriate 1D cuts, and at the same time, keeping the degeneracies. Thus, we decided to perform the RDAV-2D for the H–O–H bends and the asymmetric O–H stretches.

The generic Hamiltonian of the RDAV-1D for non-degenerate modes is shown in eqn (4), while that of the RDAV-2D for degenerate modes is shown in eqn (5).  $V(q_i)$  and  $V(q_i, q_j)$  are their respective 1D and 2D anharmonic PESs. Eqn (6) and (7) show the corresponding eigenvalue problems of eqn (4) and (5) in the matrix form:

$$\hat{H}_i^{\text{RDAV-1D}} = \frac{-\hbar^2}{2\mu_i} \frac{d^2}{dq_i^2} + V(q_i, q_{i \neq i} = 0) \quad i \in \{\phi, s_1\} \quad (4)$$

$$\hat{H}_{j,k}^{\text{RDAV-2D}} = \frac{-\hbar^2}{2} \left[ \frac{1}{\mu_j} \frac{\partial^2}{\partial q_j^2} + \frac{1}{\mu_k} \frac{\partial^2}{\partial q_k^2} \right] + V(q_j, q_k, q_{i \neq j,k} = 0) \quad (j, k) \in \{(b_1, b_2), (s_2, s_3)\} \quad (5)$$

$$\mathbf{H}_i^{\text{RDAV-1D}} |\mathbf{m}_i\rangle = \varepsilon_m^i |\mathbf{m}_i\rangle \quad i \in \{\phi, s_1\} \quad (6)$$

$$\mathbf{H}_{j,k}^{\text{RDAV-2D}} |\mathbf{n}_{j,k}\rangle = \varepsilon_n^{j,k} |\mathbf{n}_{j,k}\rangle \quad (i, j) \in \{(b_1, b_2), (s_2, s_3)\}. \quad (7)$$

In eqn (6)  $|\mathbf{m}_i\rangle$  is the  $m$ th 1D eigenvector for the non-degenerate mode  $q_i$ , its associated eigenvalue is  $\varepsilon_m^i$ . Meanwhile, in eqn (7),  $|\mathbf{n}_{j,k}\rangle$  is the  $n$ th 2D eigenvector for the degenerate modes  $q_j$  and  $q_k$ , and its associated eigenvalue is  $\varepsilon_n^{j,k}$ .

With these definitions, the PS basis  $\{|\alpha^{\text{PS}}\rangle\}$  can then be defined as follows:

$$\begin{aligned} \{|\alpha^{\text{PS}}\rangle\} &= \{|\mathbf{n}_\phi, \mathbf{m}_{b_1, b_2}, \mathbf{n}_{s_1}, \mathbf{m}_{s_2, s_3}\rangle\} \\ &= \{|\mathbf{n}_\phi\rangle \otimes |\mathbf{m}_{b_1, b_2}\rangle \otimes |\mathbf{n}_{s_1}\rangle \otimes |\mathbf{m}_{s_2, s_3}\rangle\}. \end{aligned} \quad (8)$$

Note that  $|\mathbf{n}_\phi, \mathbf{m}_{b_1, b_2}, \mathbf{n}_{s_1}, \mathbf{m}_{s_2, s_3}\rangle$  corresponds to an eigenvector for a set of four non-interacting sets of vibrational degrees of freedom. These are the hindered rotation, the degenerate H–O–H bends, the symmetric stretch, and the degenerate asymmetric stretches. Since the anharmonicity within each normal mode has already been included in eqn (4) and (5), this analysis tool, previously developed by our group,<sup>37,63</sup> is useful and efficient in describing an intermode coupling. It has been applied with great success to understand complex vibrational features in Zundel type solvated protons, which arise as a result of the strong couplings between proton stretch and flanking group motions.<sup>37</sup>

These PSs are useful in unmasking the identity of a high-dimensional vibrational eigenvector. In particular, one can expand the RDAV-6D eigenvector as a linear combination of the pure states

$$|\Psi_k\rangle = \sum_\alpha c_\alpha^k |\alpha^{\text{PS}}\rangle \quad c_\alpha^k \equiv \langle \alpha^{\text{PS}} | \Psi_k \rangle = \langle \mathbf{n}_\phi, \mathbf{m}_{b_1, b_2}, \mathbf{n}_{s_1}, \mathbf{m}_{s_2, s_3} | \Psi_k \rangle. \quad (9)$$

The inner product  $\langle \mathbf{n}_\phi, \mathbf{m}_{b_1, b_2}, \mathbf{n}_{s_1}, \mathbf{m}_{s_2, s_3} | \Psi_k \rangle$  represents the contribution of the PS to the expansion and can be evaluated provided that all  $\mathbf{H}^{\text{RDAV-1D}}$ ,  $\mathbf{H}^{\text{RDAV-2D}}$ , and  $\mathbf{H}^{\text{RDAV-6D}}$  are represented in the

same DVR basis. The square of these inner products allows us to quantitatively track each of the RDAV-6D eigenvectors back to the original set of uncoupled degrees of freedom. We will use these tools to assist us in understanding the vibrational coupling in Section 3.4.

## 2.4 Assessment of the electronic structure theory

In our previous work on  $\text{H}_3\text{O}^+\cdot\text{Ar}_n$  ( $n = 1-3$ ), our RDAV-6D calculations at the MP2/aug-cc-pVDZ level successfully explain the salient features of the spectrum measured by Johnson's group.<sup>19</sup> Furthermore, McCoy and co-workers<sup>19</sup> reported the success of MP2 in analyzing  $\text{H}_3\text{O}^+\cdot\text{X}_3$  ( $\text{X} = \text{Ar}, \text{N}_2, \text{CH}_4$ , and  $\text{H}_2\text{O}$ ). To further establish the credibility of MP2/aug-cc-pVDZ, we benchmarked the RDAV-1D and RDAV-2D frequencies at the MP2 and CCSD(T) levels of *ab initio* theory.<sup>46,64,65</sup> The comparison for  $\text{H}_3\text{O}^+\cdot\text{Ne}_3$  is shown in Table 1. At the MP2 level of theory, the difference in anharmonic frequencies between aug-cc-pVDZ and aug-cc-pVTZ is within  $30\text{ cm}^{-1}$ . Meanwhile, the RDAV-1D frequencies from MP2 and CCSD(T) using an aug-cc-pVDZ basis only differ within  $12\text{ cm}^{-1}$ . Lastly, a comparison of MP2/aug-cc-pVDZ with CCSD(T)/aug-cc-pVTZ shows that their anharmonic frequencies differ within  $45\text{ cm}^{-1}$ . In our opinion, such a small difference suggests that the MP2/aug-cc-pVDZ level of theory

and basis will suffice our purposes. With all these comparisons, we chose MP2/aug-cc-pVDZ for  $\text{H}_3\text{O}^+\cdot\text{Ne}_3$  and  $\text{H}_3\text{O}^+\cdot\text{Ar}_3$ , and MP2/aug-cc-pVDZ-PP for  $\text{H}_3\text{O}^+\cdot\text{Kr}_3$  and  $\text{H}_3\text{O}^+\cdot\text{Xe}_3$ .

## 2.5 Numerical convergence with the number of DVR grids

In our previous work on  $\text{H}_3\text{O}^+\cdot\text{Ar}_n$  ( $n = 1-3$ ), we used nine DVR grid points for each degree of freedom in constructing the 6D PES and DMS.<sup>41</sup> A total of  $9^6 = 531\,441$  grids were used to reach a convergence within  $1\text{ cm}^{-1}$ . This time, we are investigating complexes with a heavier rare gas, and the rise of computational cost in building PES and DMS is expected. As a result, we have considered the use of smaller grids. As the convergence of the calculated anharmonic frequencies with the number of grid points differs from one mode to another, we examined the peak positions for several heterogeneous sets of grid points. We have identified a smaller grid that yields results differing less than  $2\text{ cm}^{-1}$  from the results obtained using  $9^6$  grid points. From Table 2, it is evident that H–O–H bends can reach the same convergence with five grid points ( $g_{\text{bend}} = 5$ ); O–H stretches require seven grid points ( $g_{\text{stretch}} = 7$ ) and the hindered rotation (as well as the combination tones) required nine grid points ( $g_{\text{torsion}} = 9$ ). To balance accuracy and efficiency, we used the following set of grids ( $g_{\text{torsion}} \times g_{\text{bend}}^2 \times g_{\text{stretch}}^3 = 9 \times 5^2 \times 7^3$ ).

**Table 1** One-dimensional and two-dimensional anharmonic frequencies (RDAV-1D or RDAV-2D) for the six key modes in  $\text{H}_3\text{O}^+\cdot\text{Ne}_3$  at MP2 and CCSD(T) levels of theory. Note that the slight breaking of degeneracy at CCSD(T) with aug-cc-pVDZ and aug-cc-pVTZ is caused by a numerical error in the DVR scheme. Nine DVR grid points were used for each degree of freedom

RDAV- <i>n</i> D	Mode	Notation	MP2		CCSD(T)	
			aug-cc-pVDZ	aug-cc-pVTZ	aug-cc-pVDZ	aug-cc-pVTZ
1D	Hindered rotation	$\phi$	479	485	480	485
2D	H–O–H bend	$b_1$	1674	1688	1685	1699
		$b_2$	1674	1688	1685	1699
1D	Symmetric O–H stretch	$s_1$	3473	3503	3482	3516
2D	Asymmetric O–H stretch	$s_2$	3713	3716	3710	3717
		$s_3$	3713	3716	3711	3719

**Table 2** Convergence test on the peak positions (in  $\text{cm}^{-1}$ ) of the main vibration states of  $\text{H}_3\text{O}^+\cdot\text{Ar}_3$  obtained at the RDAV-6D at MP2/aug-cc-pVDZ level using different sets of DVR grids. Compared to the anharmonic frequencies obtained using  $9^6$  grids in the first column, it is obvious that the fundamental modes of bending converge to  $1\text{ cm}^{-1}$  using five DVR grids. Fundamental of stretching modes requires seven DVR grids. Hindered rotation and its combination tones are most sensitive to the number of grids. To balance accuracy and computational cost, we found a ( $g_{\text{torsion}} \times g_{\text{bend}}^2 \times g_{\text{stretch}}^3 = 9 \times 5^2 \times 7^3$ ) grid that gives sufficient accuracy with affordable computational cost

	DVR grids ( $g_{\text{torsion}} \times g_{\text{bend}}^2 \times g_{\text{stretch}}^3$ )			DVR grids			DVR grids		
Modes	$9 \times 9^2 \times 9^3$	$5 \times 5^2 \times 5^3$	Diff.	$7 \times 7^2 \times 7^3$	Diff.	$9 \times 5^2 \times 7^3$	Diff.		
Hindered rot	335.7	324.6	−11.1	332.9	−2.8	335.84	0.1		
Bending	1607.2	1606.9	−0.3	1607.2	0.0	1607.2	0.0		
Bending	1607.2	1606.9	−0.3	1607.2	0.0	1607.3	0.1		
Comb. mode	1929.7	1916.9	−12.8	1926.8	−2.9	1929.9	0.1		
Comb. mode	1929.7	1917.0	−12.7	1926.9	−2.9	1929.9	0.2		
Stretch	3163.8	3169.8	6.0	3164.3	0.5	3165.23	1.5		
Overtone bend	3184.0	3184.5	0.5	3184.1	0.1	3184.2	0.3		
Overtone bend	3184.0	3186.6	2.6	3184.2	0.2	3185.5	1.6		
Overtone bend	3230.3	3238.5	8.2	3230.9	0.6	3231.9	1.5		
Stretch	3268.5	3270.4	2.0	3268.7	0.2	3268.7	0.3		
Stretch	3268.5	3274.0	5.5	3269.0	0.5	3269.6	1.1		



A total of 77 175 single point energy evaluations were performed for each ionic cluster reported in this work.

### 3. Results and discussion

#### 3.1 Interaction of the Eigen ion ( $\text{H}_3\text{O}^+$ ) with $\text{Rg}_3$

In a very naive picture, we can imagine that each of the hydrogen atoms in  $\text{H}_3\text{O}^+$  carries a charge of  $+1/3$ . These partially charged hydrogens would interact with the Rg atoms through an ion-induced dipole. The strength of this interaction is dependent on the Rg atom's polarizability. The more polarizable Rg is, the stronger the  $\text{H}_3\text{O}^+ \cdots \text{Rg}$  binding. Since the polarizability increases with the size of the atom, we expect that the average binding strength of the  $\text{H}^{\delta+} \cdots \text{Rg}$  bond increases in the following order: Ne, Ar, Kr, and Xe. In terms of periodic table language, the  $\text{H}^{\delta+} \cdots \text{Rg}$  binding strengthens down the rare gas family.

Fig. 3 shows the electrostatic potential energy maps (ESP) for  $\text{H}_3\text{O}^+ \cdot \text{Rg}_3$ . In these maps, the deep blue regions have the most

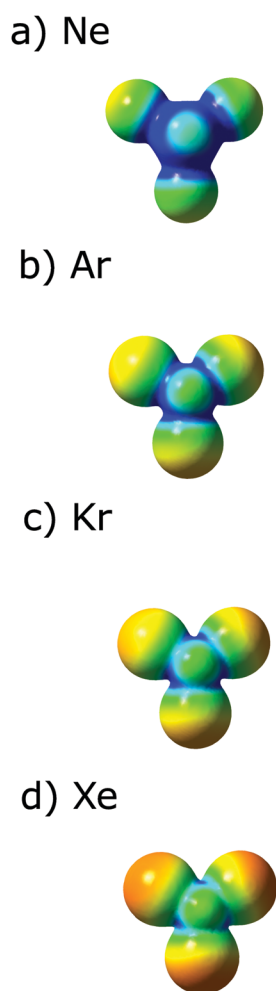


Fig. 3 Electrostatic potential maps (top view) of (a)  $\text{H}_3\text{O}^+ \cdot \text{Ne}_3$ , (b)  $\text{H}_3\text{O}^+ \cdot \text{Ar}_3$ , (c)  $\text{H}_3\text{O}^+ \cdot \text{Kr}_3$ , and (d)  $\text{H}_3\text{O}^+ \cdot \text{Xe}_3$  in their top views. The most positive regions are shaded in deep blue, while the least positive charge regions are shaded in red. Note that as the size of the rare gas increases, the positive charge distribution on the hydrogen atoms decreases. This smearing of charge implies that the complexation energy of  $\text{H}_3\text{O}^+$  with  $\text{Rg}_3$  increases down the rare gas family.

Table 3 Overall complexation energies in  $\text{kJ mol}^{-1}$  for  $\text{H}_3\text{O}^+ \cdot \text{Rg}_3$ . The complexation energy increases with the proton affinity and polarizability of the Rg atom. The overall complexation energy increases from Ne to Xe

Overall complexation energies in $\text{kJ mol}^{-1}$ for $\text{H}_3\text{O}^+ + 3\text{Rg} \rightarrow \text{H}_3\text{O}^+ \cdot \text{Rg}_3$				
Rg	Ne	Ar	Kr	Xe
Proton affinity <sup>69</sup> ( $\text{kJ mol}^{-1}$ )	198.8	369.2	424.6	499.6
Rg polarizability ( $a_0^3$ )	1.99	9.76	15.38	25.27
Complexation energy ( $\text{kJ mol}^{-1}$ )	−17.8	−47.2	−61.9	−79.4

Note: polarizability values are given for  $\alpha_{xx} = \alpha_{yy} = \alpha_{zz}$ . Numerical values for Ne and Ar are obtained at the MP2/aug-cc-pVDZ level of theory and basis, while those for Kr and Xe were calculated at the MP2/aug-cc-pVDZ-PP level of theory and basis.

positive charge and correspond to the location of the partially charged hydrogen atoms. The red regions correspond to the least positive charge. As the polarizability of the Rg increases, the partial charges carried by the hydrogens get depleted – an indication of charge smearing. This is shown by the shrinkage of the deep blue regions from Fig. 3(a)–(d). Such enhancement in charge dispersion stabilizes the  $\text{H}_3\text{O}^+ \cdot \text{Rg}_3$  complex.

To quantify the overall complexation energies, we performed a separate optimization with counterpoise correction<sup>66,67</sup> at the MP2/aug-cc-pVDZ (for  $\text{H}_3\text{O}^+ \cdot \text{Ne}_3$  and  $\text{H}_3\text{O}^+ \cdot \text{Ar}_3$ ) and MP2/aug-cc-pVDZ-PP (for  $\text{H}_3\text{O}^+ \cdot \text{Kr}_3$  and  $\text{H}_3\text{O}^+ \cdot \text{Xe}_3$ ) levels. The counterpoise scheme comprised four fragments, one fragment for  $\text{H}_3\text{O}^+$  and one fragment for each Rg. Table 3 shows the BSSE corrected complexation energies. Again, the relative stabilities of the  $\text{H}_3\text{O}^+ \cdot \text{Rg}_3$  complex are consistent with the chemical intuition based on polarizability arguments.

Alternatively, one can use the proton affinities of Rg to understand the trends in the overall complexation energies. The larger the proton affinity of Rg, the more stable the  $\text{H}_3\text{O}^+ \cdot \text{Rg}_3$  complex (see Table 3).

#### 3.2 Spectral evolution of $\text{H}_3\text{O}^+ \cdot \text{Rg}_3$ across the rare gas congeners

The vibrational spectra of  $\text{H}_3\text{O}^+ \cdot \text{Rg}_3$  (Rg = Ne, Ar, Kr, and Xe) are shown in Fig. 4. Note that the vibrational intensities below  $2000 \text{ cm}^{-1}$  are magnified ten times for easier visualization and comparison. The numerical values of these spectra are available in Table S5 of the ESI.† Three fundamental modes are expected to have frequencies above  $3000 \text{ cm}^{-1}$ . These are the symmetric O–H stretch,  $s_1$  ( $a_1$ ), and the degenerate asymmetric O–H stretches,  $s_2$  and  $s_3$  ( $e$ ). These modes are shown in blue sticks in Fig. 4(a)–(d).

The peak positions of these stretching modes are sensitive to the Rg's identity. In particular, the extent of red shift on  $\text{H}_3\text{O}^+ \cdot \text{Rg}_3$  increases from Ne to Xe. Such observation can be rationalized based on the Rg's binding energies to the partially charged  $\text{H}^+$ . As the average  $\text{H}^{\delta+} \cdots \text{Rg}$  binding energy increases from Ne to Xe, the O  $\cdots$  H $^{\delta+}$  bond slightly elongates. This elongation induces a red shift in the O–H stretching frequencies. Meanwhile, as these stretches red shift, their absorption intensities are enhanced, implying a large dipole derivative. As shown in Fig. 4(a) and (d), the asymmetric stretching modes are approximately amplified by four-fold from Ne to Xe.

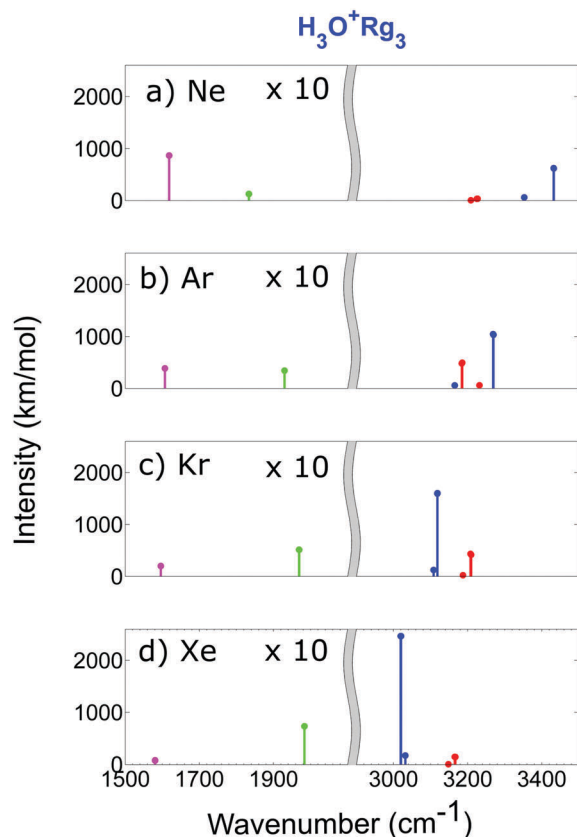


Fig. 4 The stick spectra of (a)  $\text{H}_3\text{O}^+\cdot\text{Ne}_3$ , (b)  $\text{H}_3\text{O}^+\cdot\text{Ar}_3$ , (c)  $\text{H}_3\text{O}^+\cdot\text{Kr}_3$ , and (d)  $\text{H}_3\text{O}^+\cdot\text{Xe}_3$  calculated using RDAV-6D. Sticks with dominant contributions from the fundamental and overtone H–O–H bends are depicted in pink and red respectively. Peaks with significant contributions from the fundamentals of the O–H stretches are shown in blue. The combination tones of the hindered rotation with fundamental of the H–O–H bends are depicted in light green. To compare the two spectral regions, the calculated intensities for peaks below  $2000\text{ cm}^{-1}$  are ten times magnified.

Meanwhile, the degenerate H–O–H bends are known to be less dependent on the Rg's identity. In our spectrum, fundamentals of H–O–H bend are located near  $1600\text{ cm}^{-1}$  and are shown in Fig. 4 as pink sticks. In contrast with the O–H stretches, the intensities of the H–O–H bends decline from Ne to Xe implying a decrease in the dipole derivative. A comparison of the H–O–H bend's intensities between  $\text{H}_3\text{O}^+\cdot\text{Ne}_3$  and  $\text{H}_3\text{O}^+\cdot\text{Xe}_3$  shows an approximately ten-fold reduction. Such behavior can be described using the charge sloshing phenomenon reported by McCoy<sup>19</sup> and Nesbitt.<sup>68</sup>

The frequencies for the first overtones of the H–O–H bends are expected to be around  $3200\text{ cm}^{-1}$ . As the H–O–H bends are a doubly degenerate vibration, its first overtone, which is a two quanta excitation could be  $2b_1$ , or  $2b_2$ , or  $b_1 + b_2$ . In harmonic approximation, they are expected to be triply degenerate. However, the inclusion of anharmonicity produces a splitting to this degeneracy. Transitions to these excited states are usually forbidden except in cases where they can borrow intensities from nearby fundamental bands, a phenomenon termed as Fermi resonance. Three essential conditions must be satisfied for an effective Fermi resonance. These are: (1) the

participating vibrational wave functions must belong to the same symmetry species; (2) their peak positions are nearby, that is their energy gap is small, and (3) they are coupled by a non-zero anharmonic interaction term.

The symmetry species for the first overtones of the H–O–H bend is the symmetric part of  $E \times E$  which is expressed as  $(E)^2 = A_1 + E$ . Since the stretching modes also belong to  $A_1 + E$ , the first condition is satisfied for a viable Fermi resonance.

The importance of the second condition, the matching of energy, can be seen in Fig. 4 where  $2b_1$ ,  $2b_2$ , and  $b_1 + b_2$  are shown as red sticks. In  $\text{H}_3\text{O}^+\cdot\text{Ne}_3$  (Fig. 4a), the energy difference between the  $A_1$  and  $E$  states is  $\sim 150$  and  $\sim 200\text{ cm}^{-1}$  respectively. As a result, these overtones cannot efficiently borrow intensities from  $s_2$  and  $s_3$  ( $E$ ). Meanwhile, since  $s_1$  ( $A_1$ ) has a weak oscillator strength, its intensity sharing is hardly seen. In  $\text{H}_3\text{O}^+\cdot\text{Ar}_3$  and  $\text{H}_3\text{O}^+\cdot\text{Kr}_3$  (Fig. 4b and c), there is an improvement in the energy matching between the first overtones of H–O–H bends and the O–H stretches. As a consequence, within the constraints of symmetry, the major intensity carriers ( $s_1$ ,  $s_2$ , and  $s_3$ ) can effectively impart their oscillator strengths to the  $2b_1$ ,  $2b_2$ , and  $b_1 + b_2$  peaks. However, the further red-shifting ( $\sim 3000\text{ cm}^{-1}$ ) of the O–H stretch frequencies in  $\text{H}_3\text{O}^+\cdot\text{Xe}_3$  (Fig. 5d) increases the energy mismatch leading to a decline in the acceptor's intensities. These results reveal that the Fermi resonance in  $\text{H}_3\text{O}^+$  is sensitive to the  $\text{H}^+\cdots\text{Rg}$  binding strength. The third condition, which is the anharmonic coupling term, will be quantified in Section 3.4.

Turning our attention to the lower frequency window, another feature of the complex vibrational coupling is those bands between  $1850$  and  $2000\text{ cm}^{-1}$ . In Fig. 4 these bands are represented as green sticks. The identity of this signature was assigned by McCoy and coworkers<sup>19</sup> as the combination tone of the hindered rotation with the fundamental of the H–O–H bending (*i.e.*  $\phi + b_1$  and  $\phi + b_2$ ). Our RDAV-6D calculations agree with their assignment. From Ne to Xe, this band continues to blue shift. This observation is reasonable as the hindered rotation blue-shifts with increasing solvation strength (from Ne to Xe), while the H–O–H bends hardly shift. Besides, the difference in frequency between this combination tone ( $\phi + b_1$  and  $\phi + b_2$ ) and the fundamental H–O–H bend ( $b_1$  and  $b_2$ ) is close to the hindered rotation's fundamental frequency (see Table S5 of the ESI†).

Among the Rg messengers, we found that the intensity of the combination tone (green in Fig. 4) increases significantly from Ne to Xe. In  $\text{H}_3\text{O}^+\cdot\text{Ne}_3$  the intensity of the combination tone is only  $1/6$  of the H–O–H bend (pink in Fig. 4), but in  $\text{H}_3\text{O}^+\cdot\text{Xe}_3$  the intensity becomes nine times stronger than their H–O–H bends. Moreover, the intensity of these combination tones increases consistently with that of the main intensity carriers, the O–H asymmetric stretches (blue in Fig. 5). We think that this notion gives us a strong indication on how to track the source of their intensity and we will elaborate this point in Section 3.5.

### 3.3 Exploring the nuclear quantum effects *via* H $\rightarrow$ D isotopic substitution

Vibrational spectra of  $\text{D}_3\text{O}^+\cdot\text{Rg}_3$  are compiled in Fig. 5. Numerical data for these spectra are provided in Table S6 of the ESI.† Both the hydrons and their deuteron counterparts share the

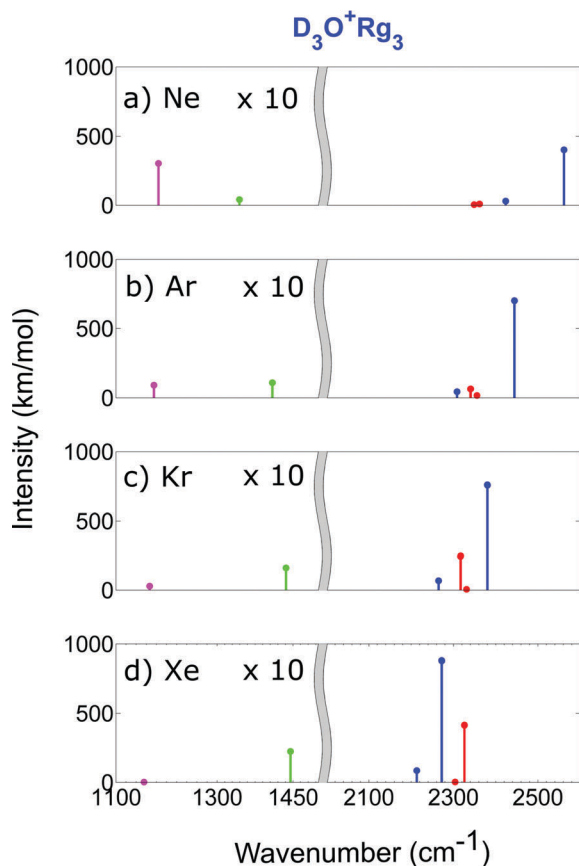


Fig. 5 The stick spectra of (a)  $\text{D}_3\text{O}^+\cdot\text{Ne}_3$ , (b)  $\text{D}_3\text{O}^+\cdot\text{Ar}_3$ , (c)  $\text{D}_3\text{O}^+\cdot\text{Kr}_3$ , and (d)  $\text{D}_3\text{O}^+\cdot\text{Xe}_3$  calculated using RDAV-6D. Sticks with dominant contributions from the fundamental and overtone H–O–H bending modes are depicted in pink and red respectively. Peaks with significant contributions from the fundamental of the O–H stretches are shown in blue. The combination tones of the hindered rotation with fundamental of the H–O–H bend are depicted in light green. To compare the two spectral regions, the calculated intensities for peaks below  $1500\text{ cm}^{-1}$  are ten times magnified.

same spectral features. From Ne to Xe, the intensities of the O–H stretches are amplified; while the intensities of the H–O–H bends are weakened. The stretching frequencies are more sensitive to the solvation strength; while the bending frequencies are virtually insensitive. The intensity of the  $\phi + b_1$  and  $\phi + b_2$  combination bands increases as it blue-shifts from Ne to Xe. Despite these similarities, the extent of Fermi resonance is different. In the hydrons, the Fermi resonance is weak in  $\text{H}_3\text{O}^+\cdot\text{Xe}_3$ , while it is strong in its deuteron counterpart,  $\text{D}_3\text{O}^+\cdot\text{Xe}_3$ . The opposite case occurs for  $\text{H}_3\text{O}^+\cdot\text{Ar}_3$ ; wherein  $\text{D}_3\text{O}^+\cdot\text{Ar}_3$  Fermi resonance is suppressed.

A comparison of the absolute intensities between  $\text{H}_3\text{O}^+\cdot\text{Rg}_3$  and  $\text{D}_3\text{O}^+\cdot\text{Rg}_3$  shows that their magnitudes are different (see Fig. 4 and 5). The absolute intensities of the former are greater than the latter. This discrepancy is caused by the difference in the scaling of the stretching and bending displacements when hydrons are replaced by deuterons. Also, the decrease in the intensity of the H–O–H bends as the Rg gets heavier is more conspicuous in  $\text{D}_3\text{O}^+\cdot\text{Rg}_3$ . From here, it can be inferred that McCoy and Nesbitt's idea on the charge sloshing effect seems to have a strong isotope dependence.<sup>19,68</sup>

Although the trends in peak positions of  $\phi + b_1$  and  $\phi + b_2$  are expected, their intensities are more interesting than in  $\text{H}_3\text{O}^+\cdot\text{Rg}_3$ . Except for  $\text{D}_3\text{O}^+\cdot\text{Ne}_3$ , the intensities of  $\phi + b_1$  and  $\phi + b_2$  (green in Fig. 5) are higher than their  $b_1$  and  $b_2$  (pink in Fig. 5). In  $\text{D}_3\text{O}^+\cdot\text{Xe}_3$  the signatures of the H–O–H bends are almost imperceptible despite a ten-fold amplification in its intensity. Meanwhile, its  $\phi + b_1$  and  $\phi + b_2$  intensities are the strongest among all the deuterons ( $\text{D}_3\text{O}^+\cdot\text{Rg}_3$ ) considered in this study.

Although the symmetries of the combination tones ( $\phi + b_1$  and  $\phi + b_2$ ) and the asymmetric O–D stretches ( $s_2$  and  $s_3$ ) belong to the same irreducible representation  $E$ , their coupling is weak due to a significant energy mismatch ( $>1000\text{ cm}^{-1}$ ). However, based on perturbation arguments, it requires a coupling strength of  $100\text{--}200\text{ cm}^{-1}$  for the combination tone to avail 1–2% of the O–D asymmetric stretches' intensities. Interestingly, the combination tones' intensities are about 1–1.7% of the total O–D asymmetric stretches' intensities. In the next section, we will quantify these couplings by using a simple two-level system.

### 3.4 Vibrational coupling in the two-level paradigm

The  $C_{3v}$  symmetry of  $\text{H}_3\text{O}^+\cdot\text{Rg}_3$  and  $\text{D}_3\text{O}^+\cdot\text{Rg}_3$  greatly simplifies the understanding of the anharmonic coupling. In this section, we offer our physical picture as well as the quantification of the anharmonic couplings described in Sections 3.2 and 3.3. We will begin by examining the Fermi resonance between the overtones and combination tones of the H–O–H bends with the fundamentals of O–H stretches.

In all of the complexes considered in this study, the  $b_1$  and  $b_2$  modes belong to the  $E$  representation. Their first overtones ( $2b_1$ ,  $2b_2$ ,  $b_1 + b_2$ ) belong to the  $A_1 + E$  representation. These excited states happened to be in the  $3000\text{--}3500\text{ cm}^{-1}$  window, where the fundamental O–H stretches ( $s_1$ ,  $s_2$ , and  $s_3$ ) are located. The  $s_1$  belongs to the  $A_1$  representation, while both  $s_2$  and  $s_3$  belong to the  $E$  representation. By vanishing integral arguments, the first overtones of the H–O–H bends having the  $E$  symmetry can only couple with  $s_2$  and  $s_3$ , while that having the  $A_1$  symmetry only couples with  $s_1$ . In  $\text{D}_3\text{O}^+\cdot\text{Rg}_3$ , the same symmetry label applies, but their peak positions are located in the range  $2100\text{--}2600\text{ cm}^{-1}$ . Fig. 6 shows the schematic diagram of these couplings.

The simplified energy diagram in Fig. 6 allows us to extract the anharmonic coupling constant ( $J$ ), and the differences in zero-order energy ( $\Delta\varepsilon$ ) arise not only from our RDAV-6D results but also from experimental measurements. Two assumptions will be made to acquire such information. First, it will be assumed that the Fermi resonance between the two  $A_1$  states is described well by a two-level system. Second, the effects of electronic anharmonicity are negligible. With these assumptions, only the peak positions ( $\tilde{\nu}_{\alpha\leftarrow 0}, \tilde{\nu}_{\beta\leftarrow 0}$ ) and absorption intensities ( $A_{\alpha\leftarrow 0}, A_{\beta\leftarrow 0}$ ) are needed to retrieve  $J$  and  $\Delta\varepsilon$ . The working equation is provided in eqn (10). Interested readers can refer to Section G of the ESI† for the derivation.

$$\Delta\varepsilon = -\sqrt{\frac{(\tilde{\nu}_{\beta\leftarrow 0} - \tilde{\nu}_{\alpha\leftarrow 0})^2}{1 + Q^2}} \quad \text{and} \quad J = \frac{Q\Delta\varepsilon}{2}, \quad (10)$$



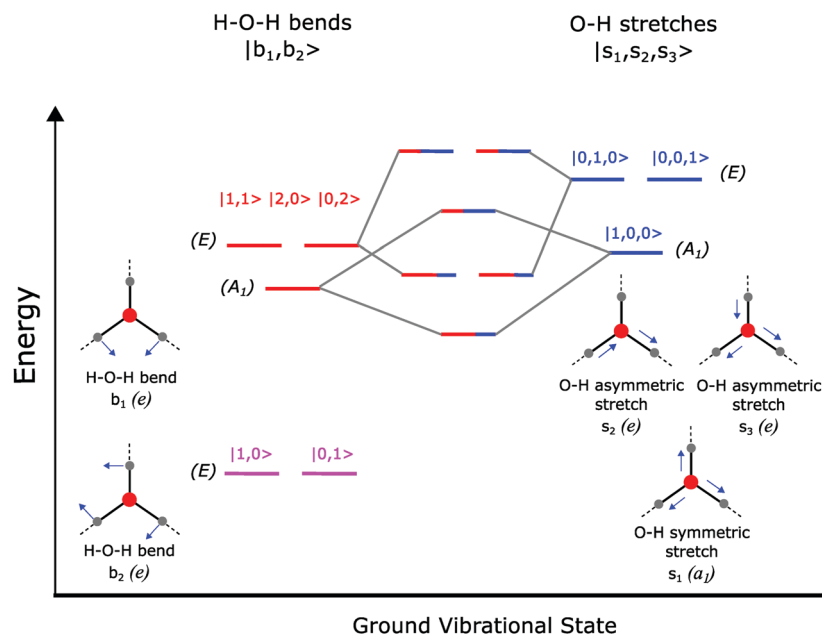


**Fig. 6** An energy diagram to summarize the key coupling between H–O–H bending and O–H stretching modes in  $\text{H}_3\text{O}^+\cdot\text{Rg}_3/\text{D}_3\text{O}^+\cdot\text{Rg}_3$ . The fundamental states for H–O–H bending belong to the  $E$  representation. The corresponding overtone states ( $2b_1$ ,  $2b_2$ , and  $b_1 + b_2$ ) belong to  $A_1 + E$ . The fundamental states for symmetric and asymmetric O–H stretches, respectively, belong to  $A_1$  and  $E$ . Only states close in energy belonging to the same irreducible representation can couple.

where

$$Q \equiv \frac{2z}{1-z^2} \quad z \equiv \sqrt{\left(\frac{A_{\beta \leftarrow 0}}{A_{\alpha \leftarrow 0}}\right) \left(\frac{\tilde{\nu}_{\alpha \leftarrow 0}}{\tilde{\nu}_{\beta \leftarrow 0}}\right)} \quad \text{and} \\ \Delta\epsilon = \epsilon_1 - \epsilon_2 \quad \epsilon_1 < \epsilon_2.$$

Meanwhile, as shown in Fig. 6, the two  $E$  states, the first overtone of H–O–H bends and fundamentals of the asymmetric O–H stretches, couple to produce two energy levels. Each level is two-fold degenerate. Intuitively, one would guess that a  $4 \times 4$  matrix is needed to describe their Fermi resonance. However, it can be proven (see Section H of the ESI†) that the  $4 \times 4$  matrix can be reduced to two identical two-level systems. Hence, eqn (10) can also be used to extract their  $J$  and  $\Delta\epsilon$  values.

The energy detuning ( $\Delta\epsilon$ ) and the anharmonic coupling constants ( $J$ ) of these complexes are compiled in Table 4. We can find that the couplings between the two  $E$  manifolds are slightly stronger than the coupling between the two  $A_1$  states. In  $\text{H}_3\text{O}^+\cdot\text{Rg}_3$ , the coupling constant between the  $A_1$  manifolds varies from 24 to  $41 \text{ cm}^{-1}$ , while those between the  $E$  manifolds ranges from 33 to  $42 \text{ cm}^{-1}$ . In other words, the anharmonic coupling among the  $A_1$  states is a bit more sensitive to the solvation environment.

In  $\text{D}_3\text{O}^+\cdot\text{Rg}_3$  the anharmonic coupling is about 2/3 of those in  $\text{H}_3\text{O}^+\cdot\text{Rg}_3$ . Focusing our attention on energy detuning, one can see that the strong Fermi resonance in  $\text{H}_3\text{O}^+\cdot\text{Ar}_3$  and  $\text{H}_3\text{O}^+\cdot\text{Kr}_3$  is due to the good frequency matching. In  $\text{D}_3\text{O}^+\cdot\text{Rg}_3$ , appropriate frequency matching occurs in  $\text{D}_3\text{O}^+\cdot\text{Kr}_3$  and  $\text{D}_3\text{O}^+\cdot\text{Xe}_3$ .

One should keep in mind that although the two-level system produces reasonable estimates on  $J$  and  $\Delta\epsilon$ , their strength lies on the validity of the two assumptions above. Furthermore,

**Table 4** Coupling constants ( $J$ ) and energy detuning ( $\Delta\epsilon$ ) (in  $\text{cm}^{-1}$ ) between O–H stretching and overtones of bending in  $\text{H}_3\text{O}^+\cdot\text{Rg}_3$  and  $\text{D}_3\text{O}^+\cdot\text{Rg}_3$  derived under the assumption of a simple two-level system. The Fermi resonance between the symmetric O–H stretch and the  $A_1$  component of the bending overtone is listed under  $A_1 \leftrightarrow A_1$ , while the Fermi resonances between two  $E$  manifolds are listed under column ( $E \leftrightarrow E$ )

Complexes	Fermi resonance type			
	$A_1 \leftrightarrow A_1$		$E \leftrightarrow E$	
	$J \text{ (cm}^{-1}\text{)}$	$\Delta\epsilon \text{ (cm}^{-1}\text{)}$	$J \text{ (cm}^{-1}\text{)}$	$\Delta\epsilon \text{ (cm}^{-1}\text{)}$
$\text{H}_3\text{O}^+\cdot\text{Ne}_3$	40.21	−119.31	41.45	−188.91
$\text{H}_3\text{O}^+\cdot\text{Ar}_3$	33.28	−1.59	39.34	−30.32
$\text{H}_3\text{O}^+\cdot\text{Kr}_3$	28.76	54.51	36.76	52.29
$\text{H}_3\text{O}^+\cdot\text{Xe}_3$	24.34	105.48	33.13	130.18
$\text{D}_3\text{O}^+\cdot\text{Ne}_3$	25.32	−54.92	29.94	−190.80
$\text{D}_3\text{O}^+\cdot\text{Ar}_3$	21.15	20.61	28.87	−86.27
$\text{D}_3\text{O}^+\cdot\text{Kr}_3$	18.65	54.70	27.29	−32.35
$\text{D}_3\text{O}^+\cdot\text{Xe}_3$	16.36	84.59	25.04	19.36

these results are expected to be very reliable provided that they form detachable (non-mixing) block matrices in the full Hamiltonian.

### 3.5 A probable cause of the association band's intensity

To examine the coupling between the hindered rotation and other degrees of freedom, we can then project the wave functions of the two intense peaks back to the pure states and examine the square of their inner products  $\langle \mathbf{n}_{\phi}, \mathbf{m}_{b_1, b_2}, \mathbf{n}_{s_1}, \mathbf{m}_{s_2, s_3} | \Psi_k \rangle$ . These squares of the inner products can then be interpreted as the weight of a given pure state in the anharmonic and coupled eigenvector. In Table 5, we compiled the list of the main contributing pure states. Indeed, the assignment of McCoy<sup>19</sup>

**Table 5** Assignments for the association band can be done by projecting their RDAV-6D eigenvectors back to the pure states. Squares of their inner products ( $|\langle \mathbf{n}_{\phi}, \mathbf{m}_{b_1, b_2}, \mathbf{n}_{s_1}, \mathbf{m}_{s_2, s_3} | \Psi_k \rangle|^2$ ) are listed in this table

	$ \mathbf{n}_{\phi}, \mathbf{m}_{b_1, b_2}, \mathbf{n}_{s_1}, \mathbf{m}_{s_2, s_3}\rangle$				$\text{H}_3\text{O}^+\cdot\text{Rg}_3$				$\text{D}_3\text{O}^+\cdot\text{Rg}_3$			
	$\mathbf{n}_{\phi}$	$\mathbf{m}_{b_1, b_2}$	$\mathbf{n}_{s_1}$	$\mathbf{m}_{s_2, s_3}$	Ne	Ar	Kr	Xe	Ne	Ar	Kr	Xe
RDAV-6D frequencies in $\text{cm}^{-1}$					1834.0	1930.0	1969.0	1983.0	1344.0	1409.0	1436.0	1445.0
RDAV-6D intensities in $\text{km mol}^{-1}$					13.0	34.0	51.0	73.0	4.0	11.0	16.0	22.0
$ \langle \mathbf{n}_{\phi}, \mathbf{m}_{b_1, b_2}, \mathbf{n}_{s_1}, \mathbf{m}_{s_2, s_3}   \Psi_k \rangle ^2$	<b>1</b>	<b>1</b>	<b>0</b>	<b>0</b>	<b>60.20</b>	<b>77.30</b>	<b>82.43</b>	<b>84.8</b>	<b>67.95</b>	<b>94.24</b>	<b>87.55</b>	<b>89.39</b>
in percent	3	1	0	0	13.97	7.10	4.64	3.61	12.63	5.22	3.46	2.64
	<b>0</b>	<b>0</b>	<b>0</b>	<b>1</b>	<b>1.42</b>	<b>2.00</b>	<b>2.29</b>	<b>2.57</b>	<b>1.11</b>	<b>1.44</b>	<b>1.58</b>	<b>1.72</b>
	3	1	1	0	5.11	2.68	1.90	1.58	4.32	2.04	1.51	1.27
	2	0	0	1	2.33	2.36	2.18	2.05	1.88	1.75	1.56	1.46

is correct; the dominating component consists of one quantum of hindered rotation and one quantum of bending. The second most significant contribution comes from the combination tones with three quanta of hindered rotation and one quantum of bending. The third largest contribution comes from the fundamental asymmetric O–H stretch. We should note here that these combination tones have *E* symmetry, which forbids the involvement of the symmetric O–H stretch. From Table 5, we can find that there are also contributions from a few other combination tones involving high excited states of the hindered rotation.

The origin of the intensity of these two combination tones can come from the mechanical and/or the electrical anharmonicity. In our computational scheme, both effects are automatically included, and it is not straightforward to separate their contributions. If we assume that the electrical anharmonicity does not play a major role, we have to look for pure states that carry intensities. From Table 5, the only set of intensity carriers that makes significant contributions are the pure states belonging to the asymmetric O–H stretch. Therefore, we also examined the intensity ratio between the combination tone and the asymmetric O–H stretch. To calculate the latter, we have also included intensities of the bending overtones as their intensities were “borrowed” from the asymmetric O–H stretch *via* Fermi resonance. The results are compiled in Table 6. We can find a strong correlation that leads us to conclude that the intensity of these combination tones can be

traced back to the asymmetric O–H stretches. The discrepancy between the %mixing and the %intensity must have come from the contributions of the electrical anharmonicity.

## 4. Conclusion

We demonstrated that by changing the solvation environment of the hydronium ion ( $\text{H}_3\text{O}^+$ ) using different types of rare gases, we could efficiently tune the coupling among its six key vibrational degrees of freedom namely, the hindered rotation, the two degenerate H–O–H bends, and the three O–H stretches. The interplay of the complex vibrational coupling results in a visible change in the spectral features that can be probed by infrared pre-dissociation (IRPD) spectroscopy. In particular, these complex and exciting spectral features as a result of the Fermi resonance in the range 3000–3500  $\text{cm}^{-1}$  for  $\text{H}_3\text{O}^+\cdot\text{Rg}_3$  and 2200–2600  $\text{cm}^{-1}$  for  $\text{D}_3\text{O}^+\cdot\text{Rg}_3$  provide a quantitative way to measure the coupling strength between the first overtone of the H–O–H bends with the fundamental of the O–H stretches. Another important feature of the vibrational coupling is the intensity of the combination tone in the range 1800–2000  $\text{cm}^{-1}$  for  $\text{H}_3\text{O}^+\cdot\text{Rg}_3$  and 1300–1500  $\text{cm}^{-1}$  for  $\text{D}_3\text{O}^+\cdot\text{Rg}_3$ . Except for Ne-tagged species, the combination tones’ intensity is stronger than their associated H–O–H bends. Based on calculated intensities, we found that the intensities of the combination tones are proportional to those of the O–H stretches. By analyzing the mixing of the wave functions in our calculations, we found that the combination tones are mixed with asymmetric O–H stretches by 1% to 3%. The ratio of intensity borrowing is consistent with the amount of mixing in the wave function. Therefore, we track the intensity of the combination tones back to the strongest intensity carriers (asymmetric O–H stretches). Although a partial isotopic substitution (*e.g.*  $\text{H}_2\text{DO}^+\cdot\text{Rg}_3$  and  $\text{HD}_2\text{O}^+\cdot\text{Rg}_3$ ) would probably give rise to more experimentally observable and exciting features, its lower symmetry will complicate the spectra, which in turn will require a more elaborate effort for their assignments. Finally, we hope that our calculations can motivate experimentalists to re-examine these complexes to verify the simple notion we learned in this work.

## Competing financial interest

The authors declare no competing financial interest.

**Table 6** Comparison between % (mixing) and % (intensity). The % (mixing) is defined as the contribution of the asymmetric O–H stretch to the  $\phi + b_1$  combination tone’s eigenvector. The % (intensity), on the other hand, is defined as the ratio of the combination tone’s intensity to the asymmetric O–H stretches’ intensity. As the intensities of the first overtone of the H–O–H bends came from the asymmetric O–H stretch, they are included in the denominator of the ratio. The strong correlation between the two percentages indicates that the combination tone’s intensity can be tracked to the asymmetric O–H stretches

Complexes	% (mixing)	% (intensity)
$\text{H}_3\text{O}^+\cdot\text{Ne}_3$	1.42	1.58
$\text{H}_3\text{O}^+\cdot\text{Ar}_3$	2.00	2.24
$\text{H}_3\text{O}^+\cdot\text{Kr}_3$	2.29	2.54
$\text{H}_3\text{O}^+\cdot\text{Xe}_3$	2.57	2.81
$\text{D}_3\text{O}^+\cdot\text{Ne}_3$	1.11	1.01
$\text{D}_3\text{O}^+\cdot\text{Ar}_3$	1.44	1.44
$\text{D}_3\text{O}^+\cdot\text{Kr}_3$	1.58	1.60
$\text{D}_3\text{O}^+\cdot\text{Xe}_3$	1.72	1.73

## Acknowledgements

This work was financially supported by various grants from Academia Sinica and the Ministry of Science and Technology (MOST) of Taiwan under MOST101-2113-M-001-023-MY3 and MOST104-2113-M-001-017. JAT would like to thank Taiwan International Graduate Program (TIGP) for a scholarship and MOST for travel support (MOST-103-2922-I-007-213). Computational resources are supported in part by the National Center for High-Performance Computing (NCHC). We wish to thank Dr Kaito Takahashi and Dr Kopin Liu for the fruitful discussions related to this project. We would like to express our gratitude to Dr Masato Morita for the DVR solver.

## References

- 1 R. P. Bell, *The Proton in Chemistry*, Chapman and Hall, London, 1973.
- 2 D. Marx, *ChemPhysChem*, 2006, **7**, 1848–1870.
- 3 D. Lancaster, M. Michel, B. Honig and M. Gunner, *Biophys. J.*, 1996, **70**, 2469.
- 4 J. Deisenhofer, O. Epp, I. Sining and H. Michel, *J. Mol. Biol.*, 1995, **246**, 429.
- 5 M. Akeson and D. Deamer, *Biophys. J.*, 1991, **60**, 101.
- 6 J. D. Lear, Z. R. Wassermann and W. F. DeGrado, *Science*, 1988, **240**, 1177.
- 7 D. T. Moore, J. Oomens, L. van der Meer, G. von Helden, G. Meijer, J. Valle, A. G. Marshall and J. R. Eyler, *ChemPhysChem*, 2004, **5**, 740–743.
- 8 T. D. Fridgen, T. B. McMahon, L. MacAleese, J. Lemaire and P. Maitre, *J. Phys. Chem. A*, 2004, **108**, 9008–9010.
- 9 K. R. Asmis, N. L. Pivonka, G. Santambrogio, M. Brümmer, C. Kaposta, D. M. Neumark and L. Wöste, *Science*, 2003, **299**, 1375–1377.
- 10 N. Heine, M. R. Fagiani and K. R. Asmis, *J. Phys. Chem. Lett.*, 2015, **6**, 2298–2304.
- 11 L. I. Yeh, M. Okumura, J. D. Myers, J. M. Price and Y. T. Lee, *J. Chem. Phys.*, 1989, **91**, 7319–7330.
- 12 M. Okumura, L. I. Yeh and Y. T. Lee, *J. Chem. Phys.*, 1988, **88**, 79.
- 13 J. M. Headrick, E. G. Diken, R. S. Walters, N. I. Hammer, R. A. Christie, J. Cui, E. M. Myshakin, M. A. Duncan, M. A. Johnson and K. D. Jordan, *Science*, 2005, **308**, 1765–1769.
- 14 G. E. Douberly, R. S. Walters, J. Cui, K. D. Jordan and M. A. Duncan, *J. Phys. Chem. A*, 2010, **114**, 4570–4579.
- 15 N. I. Hammer, E. G. Diken, J. R. Roscioli, M. A. Johnson, E. M. Myshakin, K. D. Jordan, A. B. McCoy, X. Huang, J. M. Bowman and S. Carter, *J. Chem. Phys.*, 2005, **122**, 244301.
- 16 L. R. McCunn, J. R. Roscioli, M. A. Johnson and A. B. McCoy, *J. Phys. Chem. B*, 2008, **112**, 321–327.
- 17 E. G. Diken, J. M. Headrick, J. R. Roscioli, J. C. Bopp, M. A. Johnson and A. B. McCoy, *J. Phys. Chem. A*, 2005, **109**, 1487–1490.
- 18 J. M. Headrick, J. C. Bopp and M. A. Johnson, *J. Chem. Phys.*, 2004, **121**, 11523–11526.
- 19 A. B. McCoy, T. L. Guasco, C. M. Leavitt, S. G. Olesen and M. A. Johnson, *Phys. Chem. Chem. Phys.*, 2012, **14**, 7205.
- 20 S. G. Olesen, T. L. Guasco, J. R. Roscioli and M. A. Johnson, *Chem. Phys. Lett.*, 2011, **509**, 89–95.
- 21 J. R. Roscioli, L. R. McCunn and M. A. Johnson, *Science*, 2007, **316**, 249–254.
- 22 K. Mizuse and A. Fujii, *J. Phys. Chem. A*, 2012, **116**, 4868–4877.
- 23 K. Mizuse and A. Fujii, *Chem. Phys.*, 2013, **419**, 2–7.
- 24 J. A. Fournier, C. J. Johnson, C. T. Wolke, G. H. Weddle, A. B. Wolk and M. A. Johnson, *Science*, 2014, **344**, 1009–1012.
- 25 N. I. Hammer, E. G. Diken, M. A. Johnson, R. S. Walters, T. D. Jaeger, M. A. Duncan, R. A. Christie and K. D. Jordan, *Science*, 2004, **304**, 1137–1140.
- 26 M. Miyazaki, A. Fujii, T. Ebata and N. Mikami, *Science*, 2004, **304**, 1134–1137.
- 27 C.-C. Wu, C.-K. Lin, H.-C. Chang, J.-C. Jiang, J.-L. Kuo and M. L. Klein, *J. Chem. Phys.*, 2005, **122**, 74315.
- 28 J. C. Jiang, Y. S. Wang, H. C. Chang, S. H. Lin, Y. T. Lee, G. Niedner-Schatteburg and H. C. Chang, *J. Am. Chem. Soc.*, 2000, **122**, 1398–1410.
- 29 A. B. McCoy, X. Huang, S. Carter, M. Y. Landeweer and J. M. Bowman, *J. Chem. Phys.*, 2005, **122**, 61101.
- 30 X. Huang, B. J. Braams and J. M. Bowman, *J. Chem. Phys.*, 2005, **122**, 44308.
- 31 O. Vendrell, F. Gatti and H. D. Meyer, *Angew. Chem., Int. Ed.*, 2007, **46**, 6918–6921.
- 32 O. Vendrell, F. Gatti, D. Lauvergnat and H.-D. Meyer, *J. Chem. Phys.*, 2007, **127**, 184302.
- 33 O. Vendrell, F. Gatti and H.-D. Meyer, *J. Chem. Phys.*, 2007, **127**, 184303.
- 34 O. Vendrell, M. Brill, F. Gatti, D. Lauvergnat and H.-D. Meyer, *J. Chem. Phys.*, 2009, **130**, 234305.
- 35 O. Vendrell, F. Gatti and H.-D. Meyer, *J. Chem. Phys.*, 2009, **131**, 34308.
- 36 J. A. Tan and J. L. Kuo, *J. Phys. Chem. A*, 2015, **119**, 11320–11328.
- 37 J. A. Tan and J.-L. Kuo, *Phys. Chem. Chem. Phys.*, 2016, **18**, 14531–14542.
- 38 M. Baer, D. Marx and G. Mathias, *ChemPhysChem*, 2011, **12**, 1906–1915.
- 39 B. Bandyopadhyay, T. C. Cheng and M. A. Duncan, *Int. J. Mass Spectrom.*, 2010, **297**, 124–130.
- 40 S. G. Olesen, T. L. Guasco, G. H. Weddle, S. Hammerum and M. A. Johnson, *Mol. Phys.*, 2010, **108**, 1191–1197.
- 41 J.-W. Li, M. Morita, K. Takahashi and J.-L. Kuo, *J. Phys. Chem. A*, 2015, **119**, 10887–10892.
- 42 K. Liu, *Annu. Rev. Phys. Chem.*, 2001, **52**, 139–164.
- 43 Y.-C. Li, T. Hamashima, R. Yamazaki, T. Kobayashi, Y. Suzuki, K. Mizuse, A. Fujii and J.-L. Kuo, *Phys. Chem. Chem. Phys.*, 2015, **17**, 22042–22053.
- 44 A. Fujii and K. Mizuse, *Int. Rev. Phys. Chem.*, 2013, **32**, 266–307.
- 45 M. J. Frisch, G. W. Trucks, H. B. Schlegel, G. E. Scuseria, M. A. Robb, J. R. Cheeseman, G. Scalmani, V. Barone, B. Mennucci, G. A. Petersson, H. Nakatsuji, M. Caricato, X. Li, H. P. Hratchian, A. F. Izmaylov, J. Bloino, G. Zheng, J. L. Sonnenberg, M. Hada, M. Ehara, K. Toyota, R. Fukuda,

- J. Hasegawa, M. Ishida, T. Nakajima, Y. Honda, O. Kitao, H. Nakai, T. Vreven, J. Montgomery Jr., J. E. Peralta, F. Ogliaro, M. Bearpark, J. J. Heyd, E. Brothers, K. N. Kudin, V. N. Staroverov, R. Kobayashi, J. Normand, K. Raghavachari, A. Rendell, J. C. Burant, S. S. Iyengar, J. Tomasi, M. Cossi, N. Rega, J. M. Millam, M. Klene, J. E. Knox, J. B. Cross, V. Bakken, C. Adamo, J. Jaramillo, R. Gomperts, R. E. Stratmann, O. Yazyev, A. J. Austin, R. Cammi, C. Pomelli, J. W. Ochterski, R. L. Martin, K. Morokuma, V. G. Zakrzewski, G. A. Voth, P. Salvador, J. J. Dannenberg, S. Dapprich, A. D. Daniels, Ö. Farkas, J. B. Foresman, J. V. Ortiz, J. Cioslowski and D. J. Fox, *Gaussian 09, Revision D. 01*, Gaussian, 2009.
- 46 C. Møller and M. S. Plesset, *Phys. Rev.*, 1934, **46**, 618–622.
- 47 D. Feller, *J. Comput. Chem.*, 1996, **17**, 1571–1586.
- 48 K. L. Schuchardt, B. T. Didier, T. Elsethagen, L. Sun, V. Gurumoorthi, J. Chase, J. Li and T. L. Windus, *J. Chem. Inf. Model.*, 2007, **47**, 1045–1052.
- 49 D. T. Colbert and W. H. Miller, *J. Chem. Phys.*, 1992, **96**, 1982.
- 50 J. C. Light, I. P. Hamilton and J. V. Lill, *J. Chem. Phys.*, 1985, **82**, 1400.
- 51 Z. Bacic and J. C. Light, *Annu. Rev. Phys. Chem.*, 1989, **40**, 469–498.
- 52 J. C. Light and T. Carrington, in *Adv. Chem. Phys.*, ed. I. Prigogine and S. A. Rice, John Wiley & Sons, Inc., Hoboken, NJ, USA, 2000, vol. 114, pp. 263–310.
- 53 P. W. Atkins and R. S. Friedman, *Molecular Quantum Mechanics*, Oxford University Press, New York, 4th edn, 2005.
- 54 B. E. Douglas and C. A. Hollingsworth, *Symmetry in bonding and spectra: an introduction*, Academic Press, 1985.
- 55 D. C. Harris and M. D. Bertolucci, *Symmetry and Spectroscopy: An Introduction to Vibrational and Electronic Spectroscopy*, Dover Publications, 1978.
- 56 R. S. Mulliken, *J. Chem. Phys.*, 1955, **23**, 1997.
- 57 R. S. Mulliken, *J. Chem. Phys.*, 1956, **24**, 1118.
- 58 M. Born and R. Oppenheimer, *Ann. Phys.*, 1927, **20**, 457–484.
- 59 E. B. Wilson, J. C. Decius and P. C. Cross, *Molecular Vibrations: The Theory of Infrared and Raman Vibrational Spectra*, Dover Publications, 1955.
- 60 M. Morita and K. Takahashi, *Phys. Chem. Chem. Phys.*, 2013, **15**, 14973.
- 61 J. A. Tan and J.-L. Kuo, *J. Phys. Chem. A*, 2015, **119**, 11320–11328.
- 62 A. Stathopoulos and C. F. Fischer, *Comput. Phys. Commun.*, 1994, **79**, 268–290.
- 63 J. A. Tan and J. Kuo, in *Progres in Theoretical Chemistry and Physics: Quantum Systems in Physics, Chemistry, and Biology: Selected Proceedings of QSCP-XX*, ed. A. Tadjer, R. Pavlov, J. Maruani, E. J. Brandas and G. Delgado-Barrio, Springer, 2016.
- 64 R. J. Bartlett and G. D. Purvis, *Int. J. Quantum Chem.*, 1978, **14**, 561–581.
- 65 J. A. Pople, M. Head-Gordon and K. Raghavachari, *J. Chem. Phys.*, 1987, **87**, 5968–5975.
- 66 S. Boys and F. Bernardi, *Mol. Phys.*, 1970, **19**, 553–566.
- 67 S. Simon, M. Duran and J. J. Dannenberg, *J. Chem. Phys.*, 1996, **105**, 11024.
- 68 E. S. Whitney, T. Haeber, M. D. Schuder, A. C. Blair and D. J. Nesbitt, *J. Chem. Phys.*, 2006, **125**, 54303.
- 69 D. R. Lide, *CRC Handbook of Chemistry and Physics*, Taylor & Francis, 89th edn, 2008.